14th IEA Heat Pump Conference
15-18 May 2023, Chicago, Illinois

Manuscript ID: DOEBTO-UMD-9158-23-JY1

Full Citation: Yang, J., Muehlbauer, J., Bacellar, D., Aute, V., & Hwang, Y. (2023) **Experimental Investigation of a Phase Change Material Charged Serpentine Heat Exchanger with Louvered Fins.** *14th IEA Heat Pump Conference*, May 15-18 2023.

Experimental Investigation of a Phase Change Material Charged Serpentine Heat Exchanger with Louvered Fins

Jangho YANG[a], Jan MUEHLBAUER[a], Daniel BACELLAR[a], Vikrant AUTE[a], Yunho HWANG[a*]

[1]Center for Environmental Energy Engineering
Department of Mechanical Engineering, University of Maryland
College Park, MD 20742, United States

Abstract

Phase change material heat exchangers (PCM-HX) can be used as a latent heat thermal energy storage (LHTES) component in heat pump applications to further enhance the efficiency of a heat pump as well as to yield financial savings by peak-load shifting. In this paper, a low-cost commercially available aluminum serpentine heat exchanger with louvered fins was experimentally investigated to check its thermal performance as a PCM-HX. A transparent rectangular box fabricated from acrylic plates served as a PCM container. Two cameras were used to capture the phase change process of the PCM on the front and top sides of the container during the experiment. A total of 88 installed temperature sensors throughout the test setup and a mass flow meter enabled a quantitative analysis of the PCM-HX as well. The energy balance deviation between the estimated theoretical and experimentally calculated PCM storage was ±14% considering the often-neglected heat loss and thermal mass of the PCM-HX. PCM temperature profiles, charge and discharge rates, and energy densities under different test conditions were also investigated.

Selection and/or peer-review under the responsibility of the organizers of the 14th IEA Heat Pump Conference 2023.

Keywords: Phase change material; Serpentine; Thermal energy storage; RT35HC; Experimental investigation; Louvered fins;

1. Introduction

The demands for energy-efficient heat pump technology have been steadily increasing worldwide with the goal of decreasing carbon footprints. A latent heat thermal energy storage (LHTES) integration into heat pump systems can potentially help shave the peak load demand of the residential and commercial energy sectors while using off-peak electricity, ultimately realizing both financial and energy savings. Phase change material heat exchangers (PCM-HXs) can be excellent candidates for LHTES as they can utilize the latent heat during the charging and discharging processes. When integrating LHTES into heat pump systems, heat exchanger should be designed to overcome the challenge of low thermal conductivities of PCMs. Hence, it is essential to explore different heat exchanger configuration options and expand the list of high-potential candidates that are economical and easy to implement [1]. In this paper, a commercially available serpentine tube heat exchanger with louvered fins was experimentally investigated as the first-order analysis revealed that this type of heat exchanger has a very competitive compactness and a material utilization value as compared to the other commercially available configurations such as crimped fin, wire fin, and spine fin heat exchangers. A

comprehensive thermal performance analysis including PCM temperature profiles, charge/discharge rates, energy densities, and energy balance of the PCM-HX under different operating conditions are presented in this study. Often-neglected visual observation and heat loss and thermal mass calculations were experimentally considered in the study for more of an in-depth analysis as well as to capture the practical side of the experiments. There are a number of existing literature for experimental investigations of compact PCM-HXs [1]–[4]. However, the experimental study regarding the selected heat exchanger configuration in this paper is scarce. Therefore, this study will provide one of the initial experimental data for this heat exchanger configuration when used as a PCM-HX.

2. Experimental Setup

2.1. PCM properties

RT35HC from Rubitherm [5] was chosen as a PCM for the experiments as it is known to be stable in terms of cyclic durability and has a relatively high heat storage capacity (HSC) for an organic-based PCM. Its nominal phase change temperature, thermal conductivity, specific heat, and volume expansion ratio are around 35 °C, 0.2 W/m-K, 2 kJ/kg, and 12.5%, respectively. Choosing a specific PCM with an actual hot storage applicable phase change temperature was not the main concern for this study as the main focus was to assess the thermal performance of the heat exchanger configuration itself. This statement can be further supported by the PCM heat sink topology optimization results from Ho et al. [6] where the optimization runs with PCMs with different melting temperatures yielded nearly identical optimized designs for conduction-dominated cases. Hence, the use of RT35HC in this study can be justified because if the heat exchanger showed a good performance with certain PCM, it would also show a good performance with other PCMs with different melting/solidification points for conduction-dominated cases. The original equipment manufacturer (OEM) claims that the nominal HSC within the selected temperature range is 240 kJ/kg with ±7.5% accuracy. It is important to mention that a separate differential scanning calorimetry (DSC) test was conducted to have additional reference to the enthalpy information of the PCM. The HSC values from the DSC results with a 5 °C/min heat rate yielded 180.6 kJ/kg and 203.7 kJ/kg for melting and solidification, respectively. Lastly, the total amount of PCM mass that was charged into the PCM-HX container was 3.979 kg.

2.2. PCM-to-HTF (Heat Transfer Fluid) Test Facility

An in-house test facility was used to conduct PCM-to-HTF experiments. As shown in Fig. 1, the test facility was placed inside the temperature- and humidity-controlled environmental chamber for reliable test conditions. The facility consists of main components such as Coriolis mass flow meter, gear pump, resistance heater, air-to-HTF heat exchanger with a fan, and the PCM-HX test section. T-type thermocouples and resistance temperature detectors (RTD) were installed for PCM and HTF-side temperature measurements. For HTF, deionized water was chosen for this study. The National Instruments (NI)'s data acquisition (DAQ) system together with the LabVIEW software was used for controls and data collection. It is worth mentioning the test facility could function bi-directionally using the 3-way valve and ball valves depending on the orientation of the PCM-HX. However, only one HTF direction was investigated in this study since the PCM-HX was oriented horizontally. For melting experiments, heater proportional-integral-derivative (PID) control was used to stabilize the inlet temperature of the HTF, while the air-to-HTF heat exchanger with a fan was used to control the HTF inlet temperature during the solidification experiments. The mass flow rate (MFR) was controlled by the PID control using the Coriolis mass flow meter and the pump driver during both experiments.

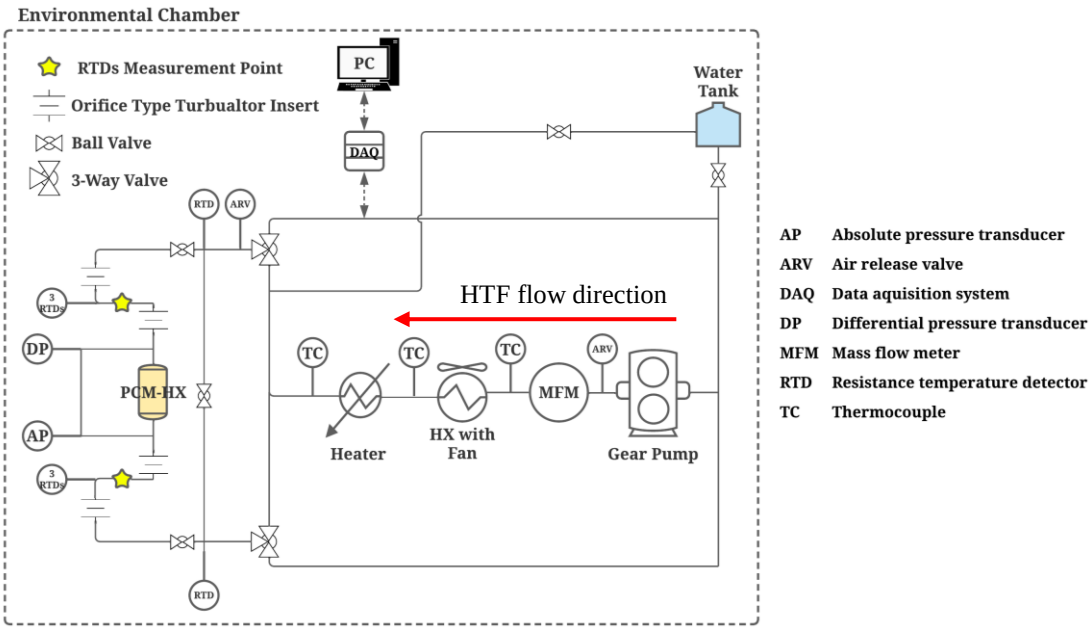

Fig. 1. PCM-to-HTF test facility schematic diagram

Sub-components such as the orifice-type turbulator inserts, 3D printed RTD guides with multi-cord grips, and 90° elbows were installed near the PCM-HX's inlet and outlet side for accurate HTF-side temperature measurement. The elbows and turbulator inserts allow the HTF to be well-mixed before the measurement points whereas the RTD guides prevent the RTD end tips from touching the tube wall and keep them concentric. Hence, the systematic uncertainties of the HTF side measurement could be minimized even with flows in a laminar regime.

2.3. Serpentine Heat Exchanger and Thermocouple Positions

A commercially available serpentine tube heat exchanger was selected as a PCM-HX candidate. A single-path serpentine tube heat exchanger consisted of 21 individual rectangular channels. The detailed dimensions and its configuration are shown in Fig. 2 – (a).

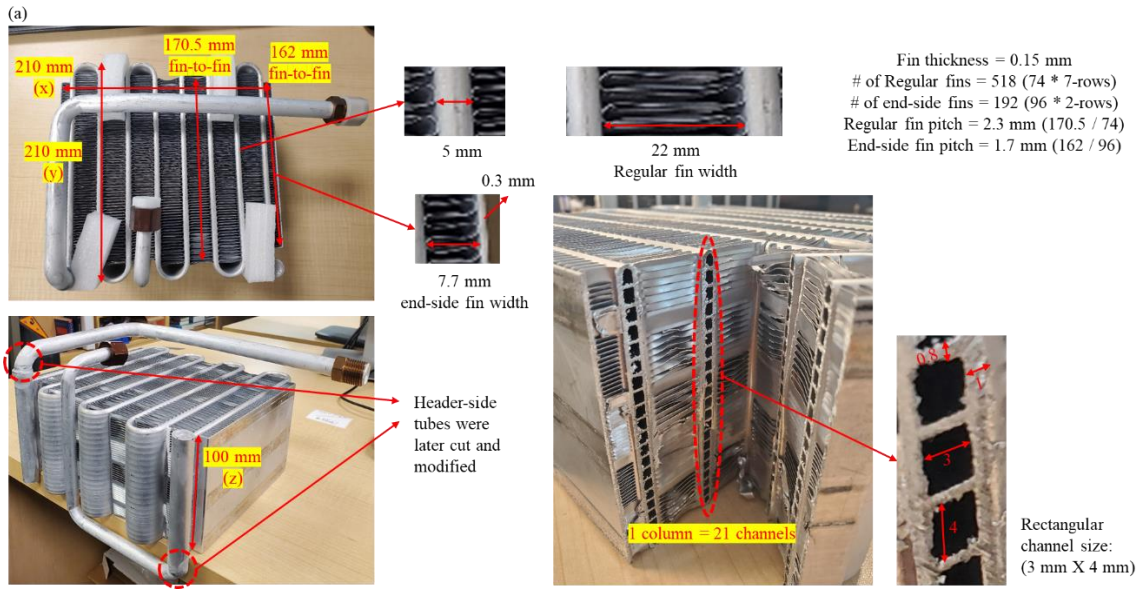

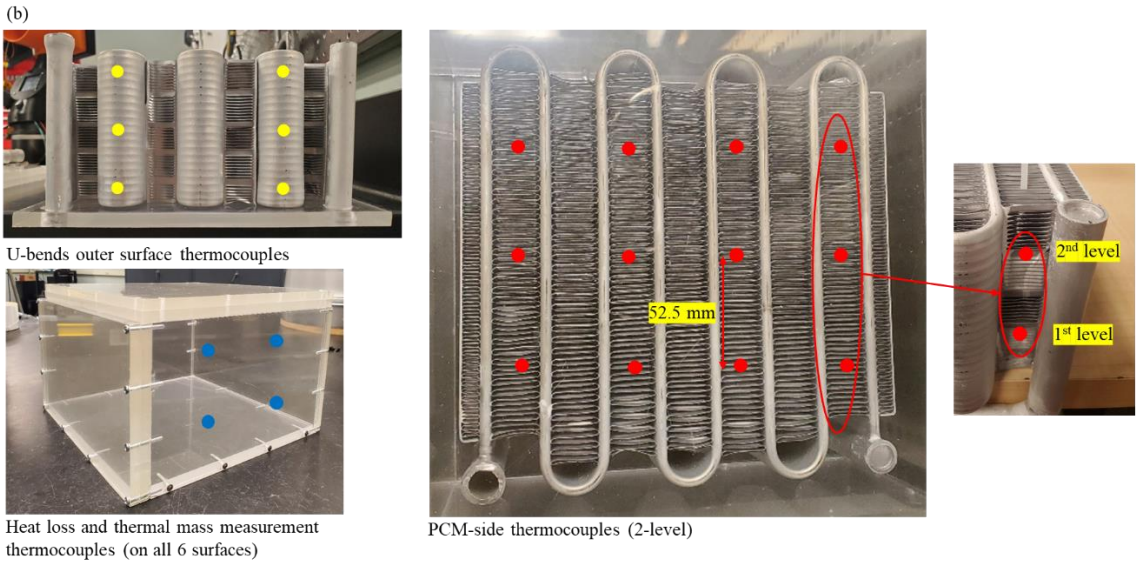

Fig. 2. (a) Serpentine tube PCM-HX dimensions and details and (b) Thermocouple distributions

In total, 78 T-type calibrated thermocouples with ±0.5 K absolute uncertainty were installed in and around the test section. After calibration, the measured maximum temperature deviation across all thermocouples was about 0.15 K when a few test points were measured. First, as shown in the top left corner of Fig. 2 - (b), six thermocouples were attached to the surfaces of the 1st and 3rd U-bends on the front side of the heat exchanger. From the bottom, the thermocouples were attached to the outer surfaces of the 3rd, 11th, and 20th rectangular channels for both U-bends. Next, as shown in the bottom left corner of the same figure, four thermocouple pairs were evenly distributed in each quadrant of the acrylic plate's inner and outer surfaces. These heat loss and thermal mass measurement thermocouples were installed on all six container surfaces. Lastly, two levels of twelve thermocouples were installed in between the fins to measure the PCM temperatures, as shown in Fig. 2 - (b). The thermocouples were installed every 52.5 mm from the front to back surfaces. The 1st and 2nd levels are 43 mm and 77 mm from the bottom surface of the container.

2.4. Container Configuration

Clear high-strength acrylic plates were used as container walls. The acrylic plates were cut to the designed dimensions using the laser cutting machine. Modified acrylic plates were later assembled with screws and acrylic epoxy for the container construction. The detailed dimensions of the container's inner volume are shown in **Error! Reference source not found.**. A 10 mm gap between the heat exchanger surfaces and the inner wall of the container was given around all heat exchanger surfaces except for the top surface. For the bottom gap, small 3D-printed blocks were attached to the bottom surface of the heat exchanger. The height of the container's inner volume was designed to have at least a 15 mm air gap at the top to prevent any unexpected PCM leakage through the top plate. The front and top surfaces used for visual observation angles were double-plated to increase the thermal resistance while maintaining transparency. The rest of the single acrylic plates were later covered with 1" thick insulation sheets.

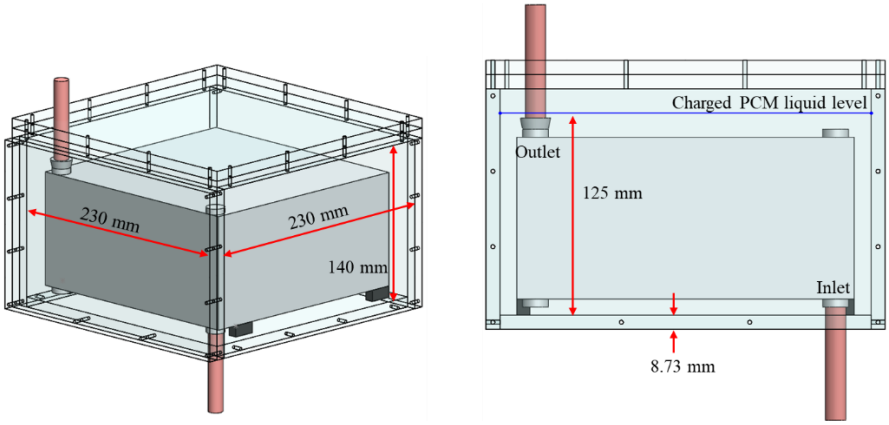

Fig. 3. A 3D model of a container and heat exchanger assembly dimensions

3. Data Reduction

The theoretical storages of the PCM-HX with the given initial and final PCM temperatures along with PCM properties were estimated using the average value of the PCM-side thermocouples temperature readings. The sensible and latent portions of the theoretical storages during both phase change processes were calculated using the temperature range that was specified by the OEM. Also, the thermal mass of the aluminum heat exchanger was considered as a part of the theoretical storage as shown in Equations (1) and (2).

$$Q_{m,theor.} = \sum M\left[C_{p,s}(27 - T_{ini.}) + L_{PCM} + C_{p,l}(T_{fin.} - 42)\right] + \sum TM_{HX} \quad (1)$$

$$Q_{s,theor.} = \sum M\left[C_{p,l}(T_{ini.} - 42) + L_{PCM} + C_{p,s}(27 - T_{fin.})\right] + \sum TM_{HX} \quad (2)$$

The accumulated HTF energies during melting and solidification were calculated using Equation (3). The time step of 10 sec was chosen as a data collecting interval.

$$Q_{(m/s),HTF} = \int_{\tau_{ini.}}^{\tau_{fin.}} \dot{m} C_{p,HTF}\left(T_{RTD_{(in/out)}} - T_{RTD_{(out/in)}}\right) d\tau \quad (3)$$

For estimating the actual charged and discharged energies, the heat loss and thermal mass considerations of the test section were necessary. Hence, Equations (4) and (5) were used. Importantly, the heat loss sum and thermal mass sum terms each contain different equations inside for charging and discharging scenarios. This was to avoid heat loss or thermal mass double counting depending on the directions of the heat transfer during each process and the defined control volumes. As this test setup only consisted of flat rectangular surfaces, a simple 1-D flat heat flow approach was assumed as shown in Equation (6).

$$Q_{charged} = Q_{m,HTF} - \sum Heat\ Loss\ - \sum Thermal\ Mass \quad (4)$$

$$Q_{discharged} = Q_{s,HTF} + \sum Heat\ Loss \pm \sum Thermal\ Mass \quad (5)$$

$$Heat\ Flow_{flat} = \int_{\tau_{ini.}}^{\tau_{fin.}} U \cdot A \cdot \Delta T\ d\tau \quad (6)$$

Moreover, Equations (7) and (8) were used to calculate the systematic uncertainties of the measured HTF side energies. The systematic uncertainties were minimized by using two sets of three 1/8-inch diameter RTDs with ±0.03 K absolute uncertainty and a Coriolis mass flow meter with ±0.2% relative uncertainty.

$$U_{Q_{water}} = \sqrt{\sum \left(\frac{\partial Q_{water}}{\partial x_i}\right)^2 U_x^2} \qquad U_{Q_{water,total}} = \sum \left(U_{Q_{water}}\right)_\tau \quad (7) \text{ and } (8)$$

Two dimensionless numbers, the Reynolds number, a ratio of fluid inertial to viscous forces, and the Stefan number [7] and [8], a ratio of sensible to latent heats were calculated using Equations (9) and (10).

$$Re = \frac{\rho u D_H}{\mu} \qquad Ste = \frac{C_{p,PCM}\left|T_{in} - T_{phase\ change}\right|}{L} \quad (9) \text{ and } (10)$$

4. Results and Discussion

4.1. Test Conditions

The summary of the test matrix is described in Table 1. The [M] and [S] in the table represent the melting and solidification cases. The test matrix was designed to test a combination of two melting inlet temperatures and three mass flow rates. The ambient temperature for all test conditions was within the range of 25.0~25.1 °C. The Reynolds numbers for a single rectangular channel for all chosen test conditions were under a laminar

flow regime due to a slow flow velocity in each channel as the main flow diverges into 21 channels. Compared with the melting cases, the solidification cases had lower Reynolds numbers as the dynamic viscosity of water increased as the water temperature decreased. The Stefan number for each test condition was also calculated to have a dimensionless parameter as a reference. The melting process was considered finished when all the heat loss and thermal mass measurement thermocouples that were installed on the inner surfaces of the acrylic plates reached 40 °C. Similarly, the solidification process was thought to be completed when the same group of thermocouples all reached 27 °C. For melting, the thermocouples located at the inner surface of the bottom acrylic reached 40 °C at last. For solidification, the thermocouples installed at the inner surface of the back-side acrylic took the longest to reach 27 °C. Importantly, the test condition 2 was repeated three times to check the test facility's repeatability before completing the test matrix, and excellent repeatability results were obtained.

The test durations and average charge and discharge rates of the PCM-HX for each test condition are shown in Table 1 as well. The higher mass flow rates yielded both faster melting and solidification and higher average charge and discharge rates. The higher average HTF inlet temperature for melting yielded faster melting, as expected. Test conditions 1 through 3 have slightly longer solidification durations than the lower average inlet T group with same MFRs as the only difference was the initial PCM temperature for the solidification process that was affected by the higher HTF inlet temperature for melting. Finally, the energy densities had negligible differences among the test conditions within the same melting HTF inlet temperature group.

Table 1. Summary of test conditions

Test	MFR [g/s]	Re for single channel	Avg. Inlet T [°C]	Ste	Test Durations [min]	Avg. Charge/Discharge rates [W]	Energy density [kWh/m^3]
1	5	143.4 [M], 78.4 [S]	58.9 [M], 26.1 [S]	0.215 [M], 0.0802 [S]	73.8 [M], 258.2 [S]	256.7 / 65.8	42.2 [M], 43.1 [S]
2	10	287.3 [M], 155.7 [S]	59.0 [M], 25.8 [S]	0.216 [M], 0.0829 [S]	62.7 [M], 224.7 [S]	299.1 / 74.8	41.8 [M], 42.0 [S]
3	15	431.0 [M], 231.9 [S]	59.0 [M], 25.5 [S]	0.216 [M], 0.0856 [S]	59.0 [M], 213.7 [S]	316.9 / 80.3	41.8 [M], 42.5 [S]
4	5	132.8 [M], 78.2 [S]	54.0 [M], 26.0 [S]	0.171 [M], 0.0811 [S]	90.5 [M], 254.3 [S]	201.6 / 61.5	40.4 [M], 39.7 [S]
5	10	265.7 [M], 156.4 [S]	54.0 [M], 26.0 [S]	0.171 [M], 0.0811 [S]	76.5 [M], 223.5 [S]	231.8 / 72.2	39.3 [M], 40.3 [S]
6	15	398.5 [M], 231.4 [S]	54.0 [M], 25.4 [S]	0.171 [M], 0.0865 [S]	73.2 [M], 212.8 [S]	242.1 / 76.2	39.3 [M], 40.3 [S]

4.2. HTF inlet Temperature, PCM Average Temperature, and ΔT

Test condition 2 from Table 1's HTF inlet temperature, PCM average temperature, and heat exchanger temperature difference between inlet and outlet are shown in Fig. 4. The HTF inlet temperature was controlled within ±1 °C during the melting process. The heater was switched off when the melting process was considered completed, then the HTF inlet temperature was brought down to the room temperature for the solidification process. The PCM average temperature was plotted using the average value of all PCM-side thermocouples. Lastly, as shown in the plot, the ΔT was measured the highest during the beginning of both melting and solidification processes, then both decreased towards to zero as the PCM absorbed and discharged most of the HTF's energy and its absorbed energy, respectively.

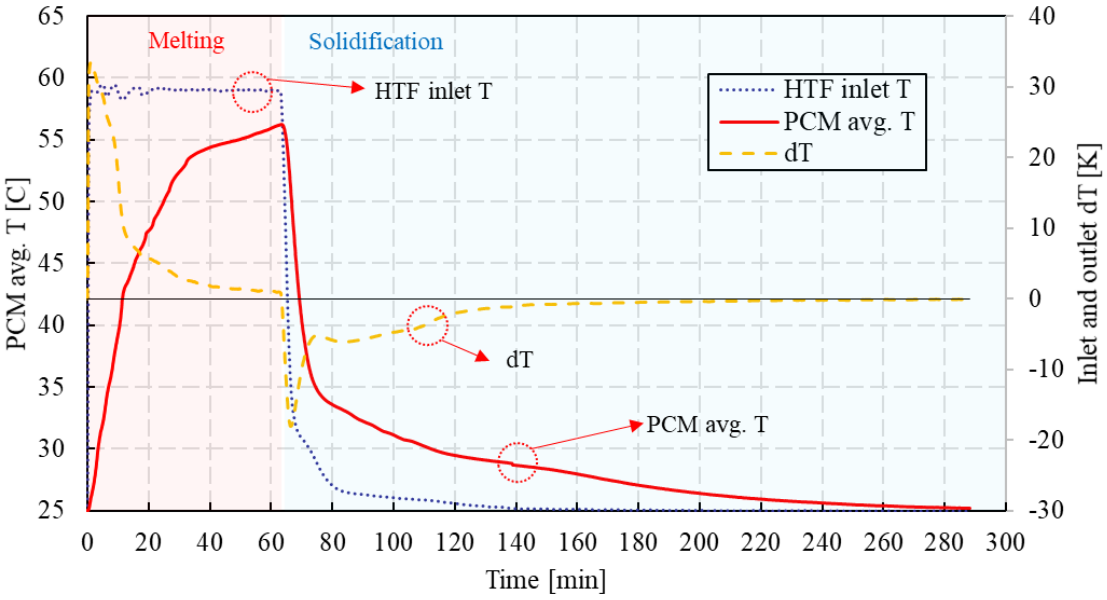

Fig. 4. Test condition 2's HTF inlet temperature, PCM average temperature, and ΔT

4.3. Visual Observation

As mentioned in section 2.4, the front and top angles were selected to visually observe the experiments. In Fig. 5, the front and top angles images of test condition 2 from Table 1 are displayed for both the melting and solidification processes. For melting, it was shown that the melting progression was from right to left and top to bottom from the front angle. It is essential to mention that the front angle view shows only the outer boundary of the PCM that touches the inner surface of the container wall. Therefore, for a more complete observation, top angle images could be investigated for comparison. The top-angle images show that the PCM in close contact with the heat exchanger surfaces quickly melted as compared with the PCM close to the container's inner walls. This could be verified by checking the ΔT plot of the heat exchanger inlet and outlet from Fig. 4 where the slope became less stiff around the 15 min mark. The charging rate slowed as only the outer PCM was left to melt. Hence, it was observed that the major portion of the PCM near the heat exchanger melted almost uniformly regardless of the height with the help of louvered fins, then the outer PCM that was closer to the container's inner walls took longer to melt due to the higher thermal resistance in the PCM layer without fins. Thus, the outer PCM melting front was from top to bottom as the melted PCM's natural convection effect was the dominant driver of heat transfer. For solidification, since conduction became the main mode of heat transfer, the solidification fronts showed more of a uniform trend that followed the serpentine path, as shown in the bottom images of Fig. 5 - (TOP) and (BOTTOM). Additionally, the PCM volume change was observed near the top section of the container as PCM solidified and increased its density, as shown in the front angle images.

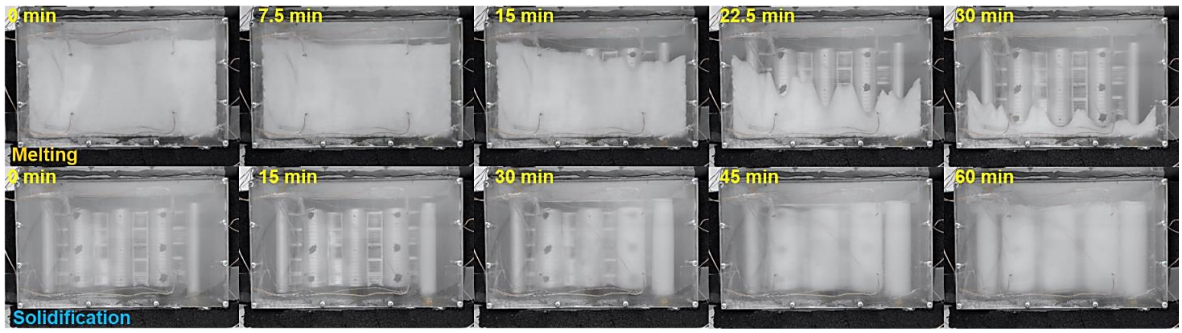

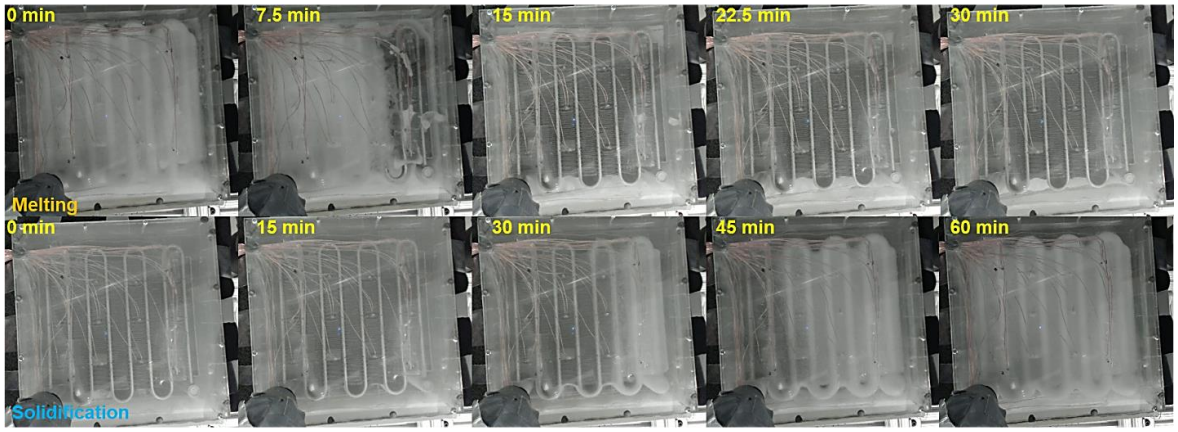

Fig. 5. Test condition 2's (TOP) front angle and (BOTTOM) top angle visual observation of first 30 mins of melting and first 60 mins of solidification

4.4. PCM Temperature Profiles

Fig. 6 – (TOP) shows test condition 2's temperature profiles for the selected PCM locations during the melting process. As shown in the image and the naming convention, the front four pairs (locations 1, 4, 7, and 10) of thermocouples were chosen for a temperature profile comparison. As mentioned in the previous section, the thermal conductivity of the PCM was largely enhanced by the louvered fins. Hence, the temperature delays between the bottom- and top-level PCM locations were relatively smaller than the vertically oriented finless PCM-HX test results from the literature [9]–[11]. The top-level PCM thermocouples started to increase the temperature gaps from the bottom-level thermocouples as the PCM around them were fully melted and the natural convection effect kicked in. Then as most of the PCM melted and their temperatures nearly reached the HTF temperature, the gaps were reduced. For all top-level PCM thermocouples, there were minor temperature dips right before they started to get flattened out, reaching the HTF temperature. This was due to the solid PCM at the top surface melting and traveling down the cracks between the fins as they became small enough to fall through. This was verified by comparing the timing of the recorded images from the top-angle camera. Also, the temperature delays across the horizontal PCM thermocouple locations were clearly shown from right to left as they followed the serpentine path.

Test condition 2's temperature profiles for the same PCM locations during the solidification process are presented in Fig. 6 – (BOTTOM). As mentioned previously, conduction became the dominant mode of heat transfer during solidification. Therefore, the temperature gaps between the bottom and top thermocouples were relatively smaller than the temperature gaps of the melting test results throughout the test. Furthermore, the temperature delays across the horizontal PCM thermocouple locations following the serpentine path were shown again during the solidification process. Lastly, a minor supercooling phenomenon was observed near 31 °C for all PCM locations.

The temperature profile data of the U-bends in different locations were also collected as well. However, for the sake of brevity, such information was not included in this study.

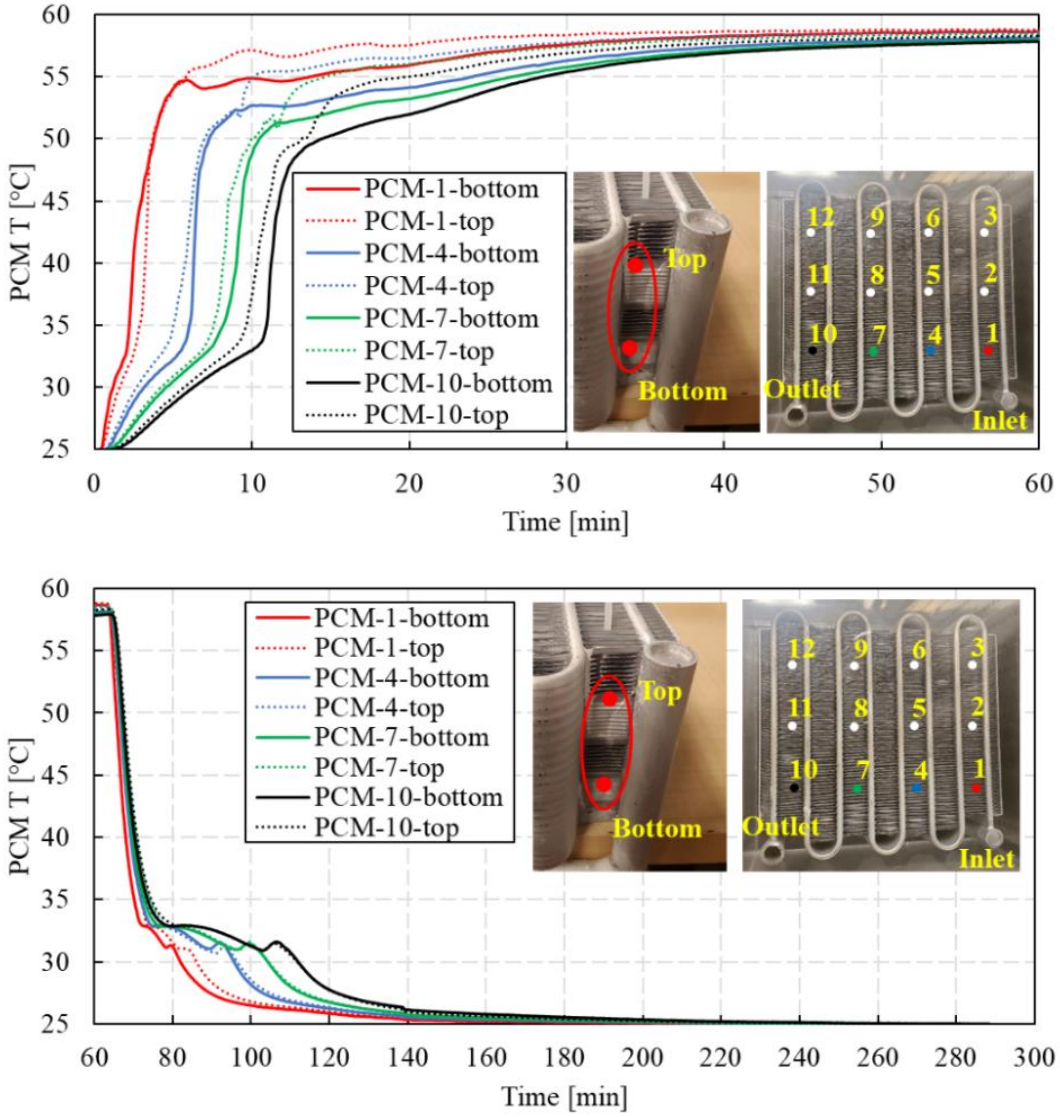

Fig. 6. Test condition 2's temperature profiles for the selected PCM locations during (TOP) melting and (BOTTOM) solidification

4.5. Energy Balance

The summary of the energy balance results for each test condition's melting [M] and solidification [S] process is presented in Table 2. The energy balance deviations were calculated using the data reduction approach in section 3. The energy balance deviation was calculated by comparing the theoretical storage and the estimated charged/discharged energy values. The average of the systematic uncertainties of the HTF (water) side energy for all test conditions was calculated to be 0.5% for melting and 1.4% for solidification, while the maximum uncertainties were 0.7% for melting and 2.1% for solidification.

Initially, although not shown here for brevity, when the nominal HSC value (240 kJ/kg) given from the OEM was used, the Q_{water} values for test conditions 2, 3, 5, and 6 during melting were smaller than their theoretical storage values which is unintuitive. The Q_{water} values contain the information of heat loss and thermal mass of the test setup on top of the PCM-HX charging process. Hence, the Q_{water} values for melting should always be larger than the theoretical storage values. Furthermore, existing literature [12]–[14] show that their in-house DSC analysis yielded 11.9%, 6.3%, and 13.8% fewer HSC values compared with the nominal value from the manufacturer's datasheet. Therefore, the HSC values from the DSC results and the lower bound of the HSC value from the OEM's datasheet were used for energy balance estimation.

As shown in the grey energy balance column, all test conditions' energy balances were within ±14% deviation when using the HSC values obtained by the DSC results. On the other hand, as presented in the green energy balance column, the melting energy balance deviations were improved significantly while the

solidification energy balance worsened when the theoretical storages were calculated using the lower bound of the HSC range. For more accurate energy balance estimation in the future, the DSC test should be conducted with multiple heat rates to get the best result as they are highly dependent on different heat rates as well as the sample size and test temperature range.

Table 2. Summary of energy balance estimation

Test	Q_{water} [kJ]	Theoretical Storage [kJ] w/ DSC HSC values	Theoretical Storage [kJ] w/ -7.5% HSC values	Estimated Charged / Discharged Energy [kJ]	Energy Balance Deviation [%] w/ DSC HSC values	Energy Balance Deviation [%] w/ -7.5% HSC values
1	1140 [M], 1020 [S]	887 [M], 979 [S]	1052 [M], 1052 [S]	1006 [M], 1025 [S]	-13.3 [M], -4.7 [S]	4.4 [M], 2.6 [S]
2	1128 [M], 1009 [S]	896 [M], 986 [S]	1061 [M], 1059 [S]	996 [M], 1000 [S]	-11.1 [M], -1.4 [S]	6.1 [M], 5.5 [S]
3	1126 [M], 1031 [S]	898 [M], 990 [S]	1063 [M], 1063 [S]	996 [M], 1012 [S]	-10.8 [M], -2.2 [S]	6.4 [M], 4.8 [S]
4	1097 [M], 938 [S]	850 [M], 940 [S]	1015 [M], 1013 [S]	961 [M], 945 [S]	-13.0 [M], -0.6 [S]	5.3 [M], 6.7 [S]
5	1067 [M], 969 [S]	854 [M], 946 [S]	1019 [M], 1019 [S]	936 [M], 960 [S]	-9.6 [M], -1.5 [S]	8.1 [M], 5.7 [S]
6	1066 [M], 974 [S]	856 [M], 947 [S]	1022 [M], 1020 [S]	937 [M], 960 [S]	-9.3 [M], -1.3 [S]	8.3 [M], 5.9 [S]

4.6. Practical Considerations

One should not only pay attention to the theoretical considerations but also carefully look into the practical considerations when implementing or designing the PCM-HX-based thermal energy storage. From this study, several practical issues were identified. One of the most common challenges with PCM-based storage is a pressure build-up in the container as the PCM undergoes a phase change process. This is caused by the volume expansion of the PCM as its density decreases as it undergoes the melting process. In this test setup, a portion of liquid PCM squirted onto the ceiling plate could be observed around the 7.5 min-mark of the melting process shown in Fig. 5 – (BOTTOM) due to the pressure build-up. Additionally, the PCM container even experienced a minor leakage issue after a number of cycles due to the repeating rounds of volume expansion and contraction cracked the acrylic epoxy adhesion. Hence, in a case where one can control the HTF direction, the HTF direction should be carefully chosen with the effort of minimizing the pressure build-up in the container. For example, one can flow the HTF downwards when the straight tube PCM-HX is oriented vertically, promoting the downwards melting trend so that the melted PCM would have a free space to expand to right away.

Another consideration that stems from the PCM volume change that one should beware of is the changing boundary condition. In a scenario where the container is narrow and long, the PCM level change during the phase changes will be relatively large. Hence, one should make sure to have the PCM-HX surfaces always submerged in the PCM during both charging and discharging modes to take full advantage of the heat transfer area.

Moreover, when initially charging the PCM liquid into the container, extra effort should be made not to create or trap any air bubbles in the container, especially in between the fins. These air bubbles can negatively affect the heat transfer between the PCM and the heat exchanger surfaces.

5. Conclusions

Overall, a PCM-HX assembly from a commercially available serpentine heat exchanger with louvered fins was embedded in RT35HC and experimentally investigated to check its thermal performance. A test matrix consisted of six test conditions with varying inlet HTF temperature and MFR. According to the obtained test results, particular conclusions were derived and can be summarized as follows:

- Increase in both Re and Ste had considerable effects on reducing the test durations while increasing the average charge and discharge rates in a laminar regime.

- For test conditions 1 to 3, the melting test durations were decreased by 15% and 20%, respectively when increasing the MFR from 5 g/s to 10 g/s and 15 g/s, whereas the solidification test duration decreased by 13% and 17%, respectively.
- For test conditions 4 to 6, the melting test durations were decreased by 15% and 19%, respectively when increasing the MFR from 5 g/s to 10 g/s and 15 g/s, whereas the solidification test duration decreased by 12% and 16%, respectively.
- For test conditions 4 to 6, the melting test durations were decreased by 18%, 18%, and 19%, respectively when the melting HTF inlet T was increased by 5 K.
- For test conditions 1 to 3, the average charge rates were increased by 16% and 23%, respectively when increasing the MFR from 5 g/s to 10 g/s and 15 g/s, whereas the average discharge rates were increased by 14% and 22%, respectively.
- For test conditions 4 to 6, the average charge rates were increased by 15% and 20%, respectively when increasing the MFR from 5 g/s to 10 g/s and 15 g/s, whereas the average discharge rates were increased by 17% and 24%, respectively.
- For test conditions 4 to 6, the average charge rates were increased by 27%, 29%, and 31%, respectively when the melting HTF inlet T was increased by 5 K.
- The energy balance deviations were within ±14% and ±9%, respectively when the HSC values from DSC results and the lower bound of the OEM datasheet were used.

In the future, for constructing a various types of PCM-HXs' performance database, the operating conditions and applications should be clearly defined so that meaningful comparisons could be made when using useful comparison approaches like rate capability and Ragone plots [15] and ε-NTU method [3], [4], [7], [16].

Nomenclature

Variables			*Subscripts*	
ρ	density	(kg/m^3)	*f*	fin
μ	dynamic viscosity	(kg/m-s)	*fin.*	final
Q	heat energy	(kJ)	*HTF*	heat transfer fluid
D_H	hydraulic diameter	(m)	*HX*	heat exchanger
L	latent heat	(m) (kJ/kg)	*ini.*	initial
M	mass	(kg)	*in*	inlet, inner
$\dot{m}$	mass flow rate	(kg/sec)	*l*	liquid state
Re	Reynolds number		*m*	melting
C_p	specific heat	(kJ/kg-K)	*out*	outlet, outer
A	surface area	(m^2)	*s*	solidification, solid state
Ste	Stefan number		*theor.*	theoretical
T	temperature	(°C)	*x*	variable
TM	thermal mass	(kJ)	*i*	variable number
τ	time step	(sec)		
U	uncertainty, U-value	(W/m^2-K)		
u	velocity	(m/s)		

Acknowledgements

The authors would like to acknowledge the funding support from the U.S. Department of Energy Award Number DE-EE0009158 and the Energy Efficiency and Heat Pump Consortium (EEHP) at the Center for Environmental Energy Engineering (CEEE), University of Maryland, College Park.

References

[1] M. Medrano, M. O. Yilmaz, M. Nogués, I. Martorell, J. Roca, and L. F. Cabeza, "Experimental evaluation of commercial heat exchangers for use as PCM thermal storage systems," *Appl. Energy*, vol. 86, no. 10, pp. 2047–2055, 2009, doi: 10.1016/j.apenergy.2009.01.014.

[2] J. P. da Cunha and P. Eames, "Compact latent heat storage decarbonisation potential for domestic hot water and space heating applications in the UK," *Appl. Therm. Eng.*, vol. 134, no. May 2017, pp.

396–406, 2018, doi: 10.1016/j.applthermaleng.2018.01.120.

[3] M. Fadl, D. Mahon, and P. C. Eames, "Thermal performance analysis of compact thermal energy storage unit-An experimental study," *Int. J. Heat Mass Transf.*, vol. 173, p. 121262, 2021, doi: 10.1016/j.ijheatmasstransfer.2021.121262.

[4] M. E. H. Amagour, A. Rachek, M. Bennajah, and M. Ebn Touhami, "Experimental investigation and comparative performance analysis of a compact finned-tube heat exchanger uniformly filled with a phase change material for thermal energy storage," *Energy Convers. Manag.*, vol. 165, no. December 2017, pp. 137–151, 2018, doi: 10.1016/j.enconman.2018.03.041.

[5] "RT35HC Data Sheet," Rubitherm Technologies, 2020. https://www.rubitherm.eu/media/products/datasheets/Techdata_-RT35HC_EN_09102020.PDF.

[6] J. Y. Ho, Y. S. See, K. C. Leong, and T. N. Wong, "An experimental investigation of a PCM-based heat sink enhanced with a topology-optimized tree-like structure," *Energy Convers. Manag.*, vol. 245, 2021, doi: 10.1016/j.enconman.2021.114608.

[7] Z. Khan and Z. A. Khan, "Thermodynamic performance of a novel shell-and-tube heat exchanger incorporating paraffin as thermal storage solution for domestic and commercial applications," *Appl. Therm. Eng.*, vol. 160, no. January, 2019, doi: 10.1016/j.applthermaleng.2019.114007.

[8] R. E. Murray and D. Groulx, "Experimental study of the phase change and energy characteristics inside a cylindrical latent heat energy storage system: Part 1 consecutive charging and discharging," *Renew. Energy*, vol. 62, pp. 571–581, 2014, doi: 10.1016/j.renene.2013.08.007.

[9] J. Yang, J. Muehlbauer, D. Bacellar, V. Aute, and Y. Hwang, "Experimental Investigation of Melting and Solidification Processes of Phase Change Material Heat Exchanger," 2021, doi: 10.18462/iir.PCM.2021.2034.

[10] D. S. Mehta, K. Solanki, M. K. Rathod, and J. Banerjee, "Thermal performance of shell and tube latent heat storage unit: Comparative assessment of horizontal and vertical orientation," *J. Energy Storage*, vol. 23, no. March, pp. 344–362, 2019, doi: 10.1016/j.est.2019.03.007.

[11] M. Longeon, A. Soupart, J. F. Fourmigué, A. Bruch, and P. Marty, "Experimental and numerical study of annular PCM storage in the presence of natural convection," *Appl. Energy*, vol. 112, pp. 175–184, 2013, doi: 10.1016/j.apenergy.2013.06.007.

[12] M. Kraiem, M. Karkri, S. Ben Nasrallah, P. Sobolciak, and M. Fois, "Thermophysical characterization and numerical investigation of three paraffin waxes as Latent Heat Storage Materials .," *Energy fuel Technol.*, no. March, 2019, doi: 10.20944/preprints201903.0034.v1.

[13] T. Barz, J. Krämer, and J. Emhofer, "Identification of phase fraction⇓temperature curves from heat capacity data for numerical modeling of heat transfer in commercial paraffin waxes," *Energies*, vol. 13, no. 19, 2020, doi: 10.3390/en13195149.

[14] H. İ. Yamaç and A. Koca, "Experimental investigation of water flow window system and numerical modeling of solar thermal energy storage with phase change materials on the way of nearly zero energy buildings," *J. Energy Storage*, vol. 43, no. September, 2021, doi: 10.1016/j.est.2021.103118.

[15] J. Woods, A. Mahvi, A. Goyal, E. Kozubal, A. Odukomaiya, and R. Jackson, "Rate capability and Ragone plots for phase change thermal energy storage," *Nat. Energy*, vol. 6, no. 3, pp. 295–302, 2021, doi: 10.1038/s41560-021-00778-w.

[16] N. H. S. Tay, M. Belusko, and F. Bruno, "An effectiveness-NTU technique for characterising tube-in-tank phase change thermal energy storage systems," *Appl. Energy*, vol. 91, no. 1, pp. 309–319, 2012, doi: 10.1016/j.apenergy.2011.09.039.